Intermodal synchronization effects in multimode fibers with noninstantaneous nonlinearity

Chao Mei [1,2] Günter Steinmeyer [2,3] Jinhui Yuan [1,4,*] Xian Zhou,[1] and Keping Long[1]

[1]*Research Center for Convergence Networks and Ubiquitous Services, University of Science and Technology Beijing, 100083 Beijing, China*
[2]*Max Born Institute for Nonlinear Optics and Short Pulse Spectroscopy, Max-Born-Straße 2a, 12489 Berlin, Germany*
[3]*Institut für Physik, Humboldt Universität zu Berlin, Newtonstraße 15, 12489 Berlin, Germany*
[4]*State Key Laboratory of Information Photonics and Optical Communications, Beijing University of Posts and Telecommunications, Beijing 100876, China*

The synchronization of spatial modes in the formation of multimode solitons can be considered as the transverse analog of mode locking. In this process, the inherent Kerr nonlinearity in the fiber core binds different spatial fiber modes together. However, compared to their temporal counterparts, the binding mechanism in multimode solitons is rather weak and susceptible to perturbation. In order to mitigate this effect, the propagation in multimode fibers with noninstantaneous Kerr media (NKM) is theoretically investigated. Our study focuses on the dynamics of intermodal energy transfer for the two cases of weak and strong walk-off. Both the moment method and numerical simulations of a multimode expansion of the nonlinear Schrödinger equation are employed. Scenarios of pure, hybrid, and varying NKM are investigated. For pure NKM, it is found that for weak walk-off, higher order spatial modes are accelerated in the time domain when their energy is transferred to lower order modes, that is, an effect that has previously been discussed as self-cleaning. In the hybrid case, when an additional instantaneous Kerr effect is present, this results in an enhancement of intermodal nonlinear coupling, leading to prominent oscillating evolutions of the derivatives of energy and pulse center. For varying NKM, the nonlinear refractive index and the proportion of noninstantaneous Kerr nonlinearity may both vary with pulse width. In this case, energy transfer and temporal shift are essentially determined by the magnitude of nonlinear response time of NKM. Significant temporal self-splitting at the trailing edge is observed for the lowest order mode provided only that the response time is large enough and irrespective of strong or weak walk-off.

I. INTRODUCTION

Solitons in multimode optical fibers have been studied for more than 40 years [1]. Compared to their counterparts in single-mode fibers, stable propagation of multimode solitons is substantially more difficult to maintain given the adverse intermodal walk-off and cross-phase modulation (XPM) effects. As a result, these transverse effects may easily interfere with the careful balance between dispersion and nonlinearity required for stable propagation of the temporal soliton. Hasegawa already showed that multimode solitons require significantly higher peak powers for their support compared to single-mode soliton. This requirement was explained by the creation of a deeper spatial potential well necessary to confine multimode wave packets [1]. Subsequent theoretical analysis showed that XPM plays an important role in the formation of multimode solitons as it fosters localization of spatiotemporal wave packets [2,3]. While this pioneering work already predicted the existence of multimode solitons, experimental evidence did not appear until 2013 [4]. In the latter experiments, spatiotemporal solitonic wave packets were observed in multimode fibers, which were designed to support a controlled number of transverse modes. Compared to the propagation of single-mode solitons, numerical modeling of multimode solitons is significantly more complicated because of the rich spatiotemporal effects in multimode fibers. As one such example, self-imaging has been reported for transverse fields when the respective self-imaging period is smaller than the dispersion length L_D [5,6]. Spatial self-cleaning is another effect that may appear in the multimode-soliton scenario, with an irreversible transfer of energy from high-order spatial modes into the fundamental one [7]. The Kerr nonlinearity has been discussed as one possible explanation for self-cleaning [8], yet stimulated Raman scattering [9] or stimulated Brillouin scattering [10] have also been discussed as possible drivers behind the self-cleaning. In particular, Raman scattering in combination with the Kerr effect can be understood as a hybrid Kerr nonlinearity, consisting of an instantaneous and a delayed response. Regardless of the exact mechanism, the initial energy distribution among the transverse modes contracts into the fundamental mode, which leads to a decrease of beam diameter. In the case of Raman-assisted transfer, it has been recently argued that the soliton self-frequency shift contributes to a group velocity match between higher order and lower order modes [11]. Another approach toward understanding the dynamics of the multimode system is rooted in thermodynamics and nonlinear dynamics. To this end, one assumes that the fundamental spatial mode acts as an attractor of

the multimode system. In this picture, high-order modes then experience a thermalization that irreversibly evolves toward the attractor state, i.e., the lowest order mode [12,13].

Apart from the aspect of energy transfer, temporal dynamics also require some scrutiny. When energy flows from higher order to lower order modes, soliton fission may take place due to the rapidly increased soliton order in the lower order modes [14]. Additionally, intermodal group delay may serve to cause a temporal breakup between different modes [15]. Controlling the differential group delay, solitons may trap or repel each other, depending on the intensity of walk-off effects [16]. Higher order modes can also be trapped in the temporal potential well created by lower order modes when the walk-off is relatively weak.

While multimode solitons in instantaneous Kerr media have been studied intensively, noninstantaneous Kerr media (NKM) offer some potential to effectively increase the nonlinearity and mitigate the rather pronounced phase-matching issues. In silica fibers, the noninstantaneous contribution stems from Raman scattering and is caused by atomic vibration. A recent study showed that Raman-induced temporal delay can be enhanced in multimode fibers [17] even though Raman scattering only contributes a small part to the nonlinearity, i.e., 18% in silica. Stronger effects can be observed in photonic crystal fibers that were filled with a Raman-active gas, giving rise to pronounced modulation effects in the spectral and temporal domain [18]. Finally, exploiting the reorientational Kerr effect in molecular liquids like CS_2 [19,20] leads to giant nonlinearities, yet at the expense of time constants that are orders of magnitude beyond those of electronic Kerr nonlinearities. In contrast to the role of the Raman effect in silica, the noninstantaneous Kerr nonlinearity in molecular liquids now prevails in the dynamics. Previously, localized noninstantaneous solitons have been reported in a pure NKM (i.e., lacking any istantaneous effect) when the input pulse duration is much shorter than molecular relaxation time [21]. Strictly speaking, the noninstantaneous soliton reported in Ref. [21] has to be taken with a grain of salt as the reported soliton solution is only an approximate result. Recent studies showed that pure NKM solitons differ from the usual hyperbolic secant shape [22] and localized solutions rather appear for Airy or Pearcey input pulse shapes [23,24]. When both instantaneous and noninstantaneous nonlinearities participate, the resulting solitonic wave packet is usually referred to as hybrid soliton [25]. Compared to the instantaneous Kerr nonlinearity, the noninstantaneous solitons often show different behavior in nonlinear interactions. For example, modulation instability in NKM can be strongly affected by nonlinear coupling between two copropagating pulses [26,27]. Dispersive wave generation, four-wave mixing (FWM) [28], soliton fission [29], and supercontinuum generation [30] under noninstantaneous circumstances also often display peculiar nonlinear dynamics. Moreover, to the best of our knowledge, the dynamics of multimode soliton propagation in NKM has not been studied yet.

In the following, the intermodal synchronization effects of multimode solitons propagation in NKM are investigated in detail by using the moment method [31,32]. The results are then further verified by numerical simulations. Given that the proportion of noninstantaneous Kerr nonlinearity and magnitude of response time in NKM can be varied, e.g., through the choice of material, we study pure, hybrid, and varying NKM by using a generalized nonlinear Schrördinger equation (GNLSE). Going beyond previous work, we focus on energy transfer and temporal shift along propagation when walk-off effects are either strong or weak. The influence of instantaneous Kerr nonlinearity on energy transfer and temporal shift is studied by varying the pure NKM to hybrid NKM. Furthermore, a pulse width-dependent noninstantaneous Kerr nonlinearity in varying NKM is also studied as an alternative approach to this problem. To this end, two different response times are studied in the simulation for comparison under strong or weak walk-off.

II. THEORETICAL FRAMEWORK

The nonlinear propagation of multimode pulses in pure NKM, involving both intermodal XPM and FWM, is modeled by a multimode expansion of the well-known nonlinear Schrödinger equation, which has evolved to a standard method for simulating nonlinear optical propagation in multimode fibers [3,4,33,34]. In the following, we refer to this equation as the multimode GNLSE. Here we adopt a slightly simplified version [35], which assumes a slow variations of noninstantaneous response and pulse envelope compared to the cycle of the carrier wave. Moreover, frequency-dependent mode functions are omitted to make our model more easily tractable. After normalization, our model equation is written as

$$
\frac{\partial u_p}{\partial \xi} = id_{0p}u_p - d_{1p}\frac{\partial u_p}{\partial \tau} - i\frac{d_{2p}}{2}\frac{\partial^2 u_p}{\partial \tau^2} + iN_s^2
$$
$$
\times \sum_{lmnp} f_{\ell mnp} u_\ell [\mathcal{R}(\tau) \otimes (u_m u_n^*)], \quad (1)
$$

where $u(\tau, \xi) = A(\tau, \xi)/\sqrt{P_N}$, $A(\tau, \xi)$ is the electric-field amplitude, and P_N is the peak power used for normalization. The latter equals to the peak power of the fundamental soliton in the fundamental fiber mode. Subscripts ℓ, m, n, and $p \in \{1, 2, 3\}$, referring to the involved three modes. All modes are considered linearly polarized. To normalize the propagation distance z, we define the dispersion length of the lowest order mode as $L_D = T_0^2/\beta_{21}$. Here T_0 is the initial pulse width in the three modes, and β_{21} is the group-velocity dispersion of the lowest order mode. $\xi = z/L_D$ and $\tau = t/T_0$ are the normalized propagation distance and time, respectively, and t is the absolute time. The propagation constant of the pth mode can be expanded as a Taylor series

$$
\beta_p(\omega) = \beta_{0p} + \beta_{1p}(\omega - \omega_0) + \beta_{2p}(\omega - \omega_0)^2/2 + \cdots, \quad (2)
$$

where β_{0p}, $\beta_{1p} = (d\beta_p/d\omega)|_{\omega=\omega_0}$ and $\beta_{2p} = (d^2\beta_p/d\omega^2)|_{\omega=\omega_0}$ specify the propagation constant, the group delay, and its dispersion for the pth mode, respectively. Additionally we define $d_{0p} = (\beta_{0p} - \beta_{01})L_D$ as the differential propagation constant between the pth and the fundamental mode. Here we neglect higher order dispersion effects as most of the interesting dynamics appears on length scales of a few L_D and because our pulses are relatively long, i.e., $T \geqslant 100$ fs. Based on an exact computation [36] of propagation constants for a multimode fiber with 50 μm

TABLE I. Overlap integrals between M1, M2 and M3

Modes	Overlap integrals	Value
M1, M2, M3	$f_{1111}, f_{2222}, f_{3333}$	1, 3/4, 1/2
M1 $\leftrightarrow$ M2	$f_{1212}, f_{2211}, f_{1122}, f_{2121}$	1/2, 1/2, 1/2, 1/2
M1 $\leftrightarrow$ M3	$f_{1313}, f_{3311}, f_{1133}, f_{3131}$	1/4, 1/4, 1/4, 1/4
M2 $\leftrightarrow$ M3	$f_{2323}, f_{3322}, f_{2233}, f_{3232}$	1/8, 1/8, 1/8, 1/8

core diameter and 0.02 index step, we determined $d_{01} = 0$, $d_{02} = -1$, and $d_{03} = -3$ as a reasonable model assumption; i.e., the phase mismatch between the modes grows with mode number. In addition to the primary phase-mismatching effect, we define differential group delay and also a group-velocity dispersion mismatch for pth mode as $d_{1p} = (\beta_{1p} - \beta_{11})L_D/T_0$ and $d_{2p} = \beta_{2p}/|\beta_{21}|$, respectively. As the importance of these effects decreases with the order number, we neglect higher order dispersion effect. We further neglect losses due to scattering or bending losses as they play no important role on the short propagation length we consider in the following. We further assume $d_{11} = 0$ and $d_{21} = -1$; i.e., we chose the reference frame of the fundamental mode and assume anomalous dispersion. N_s is the soliton order, again normalized to the fundamental mode. We finally define overlap integrals $f_{\ell mnp}$. These factors govern the intermodal nonlinear coupling. The value of $f_{\ell mnp}$ is derived from the spatial field $F(x, y)$ via

$$f_{\ell mnp} = \frac{1}{A_N} \int_{-\infty}^{\infty} F_\ell^* F_m F_n F_p^*. \tag{3}$$

Here both A_N and f_{1111} are set to unity. Since ℓ, m, n, p may vary from 1 to 3, there is a total of 81 overlap integrals in total. However, most of them vanish and do not contribute to intermodal nonlinear coupling [37,38]. Therefore, we restrict ourselves to the 15 largest overlap integrals in this work; see Table I. Here M1, M2, and M3 refer to the fundamental, second, and third modes, respectively. The symbol $\otimes$ in Eq. (1) represents a convolution in the time domain. The noninstantaneous Kerr nonlinearity is generally characterized by a response function $\mathcal{R}(\tau)$. For NKM liquids like CS_2, $\mathcal{R}(\tau)$ is derived from the Debye-Stokes-Einstein relation as a sum of harmonic oscillator function with individual ex-

ponential rise and decay functions. These three functions represent the model molecular reorientation, librational response, and intermolecular collision-induced variations [20]. While a compound model might provide a more complete description of noninstantaneous effects, we decided to resort to a simpler model that only includes Debye-type relaxation, following up on Refs. [21,39]. The noninstantaneous response function $\mathcal{R}(\tau)$ is generally written as $\mathcal{R}(\tau) = \Theta(\tau)h(\tau)$ with $h(\tau) = \exp(-\tau/T)/T$, where T is the response time and $\Theta(\tau)$ is the Heaviside function. In highly NKM, $T \gg \tau_0$, where $\tau_0 = 1$ is the normalized pulse width. While our 1D+1 GNLSE does not include the space-time coupling like 2D+1 variants [40–43], resulting self-steepening effects appear negligible in our analysis of walk-off effects between fiber modes at rather long pulse durations. Moreover, as our multimode expansion only involves three modes, it is numerically much less expensive than 2D+1 or even 3D+1 approaches and therefore allows effective scanning of a much larger parameter space in relatively short computation time.

For deeper understanding of the dynamics of intermodal interaction, we employ the moment method to analyze the evolution of energy and pulse center upon propagation. The moment method is a semianalytic method, which provides qualitative descriptions of nonlinear dynamics. This method has been widely used in the study of temporal and spectral shifts [31,32] in the single-mode case. For the opposite case of multiple modes, energies of M1, M2, and M3 are written as

$$E_\ell(\xi) = \int_{-\infty}^{\infty} |u_\ell(\xi)|^2 d\tau, \tag{4}$$

with $\ell = 1, 2$, and 3, respectively. Accordingly, the energy derivatives for the three modes can be calculated from Eq. (4)

$$\frac{dE_\ell}{d\xi} = \int_{-\infty}^{\infty} \left(u_\ell^* \frac{du_\ell}{d\xi} + u_\ell \frac{du_\ell^*}{d\xi} \right) d\tau. \tag{5}$$

Substituting Eq. (1) and its conjugated equation into Eq. (5), all differential terms in Eq. (5) on the right-hand side can now be eliminated. Taking M1 as an example, the new expression for the energy derivative containing N_s and $f_{\ell mnp}$ is then written as

$$\frac{dE_1}{d\xi} = iN_s^2 \int_{-\infty}^{\infty} \{(f_{2211}u_1^*u_2 - f_{2121}u_1u_2^*)[\mathcal{R} \otimes (u_2u_1^*)] + (f_{2121}u_1^*u_2 - f_{2211}u_1u_2^*)[\mathcal{R} \otimes (u_2^*u_1)]$$
$$+ (f_{3311}u_1^*u_3 - f_{3131}u_1u_3^*)[\mathcal{R} \otimes (u_3u_1^*)] + (f_{3131}u_1^*u_3 - f_{3311}u_1u_3^*)[\mathcal{R} \otimes (u_3^*u_1)]\}d\tau. \tag{6}$$

Equation (6) can be further simplified by only considering the fundamental soliton, i.e., $N_s = 1$. Substituting all values of $f_{\ell mnp}$ listed in Table I into Eq. (6), we yield

$$\frac{dE_1}{d\xi} = i \int_{-\infty}^{\infty} \left\{ \frac{u_1^*u_2 - u_1u_2^*}{2}[\mathcal{R} \otimes (u_1^*u_2 + u_1u_2^*)] + \frac{u_1^*u_3 - u_1u_3^*}{4}[\mathcal{R} \otimes (u_3u_1^* + u_1u_3^*)] \right\} d\tau. \tag{7}$$

In the same fashion, energy derivatives of M2 and M3 compute as

$$\frac{dE_2}{d\xi} = i \int_{-\infty}^{\infty} \left\{ \frac{u_2^*u_1 - u_2u_1^*}{2}[\mathcal{R} \otimes (u_1u_2^* + u_2u_1^*)] + \frac{u_2^*u_3 - u_2u_3^*}{8}[\mathcal{R} \otimes (u_3u_2^* + u_2u_3^*)] \right\} d\tau \tag{8}$$

and

$$\frac{dE_3}{d\xi} = i \int_{-\infty}^{\infty} \left\{ \frac{u_3^*u_1 - u_3u_1^*}{4}[\mathcal{R} \otimes (u_1u_3^* + u_3u_1^*)] + \frac{u_2u_3^* - u_3u_2^*}{8}[\mathcal{R} \otimes (u_3u_2^* + u_2u_3^*)] \right\} d\tau. \tag{9}$$

During propagation, the envelope functions of M1, M2, and M3 are defined as $\mathcal{F}_1(\tau - \tau_{c1})$, $\mathcal{F}_2(\tau - \tau_{c2})$, and $\mathcal{F}_3(\tau - \tau_3)$, where τ_{c1}, τ_{c2}, and τ_{c3} are the centers of gravity of the respective envelope function. While the input wave forms for three modes are all hyperbolic secants, subsequent propagation gives rise to a deformation of their temporal profiles because of intermodal interactions. Based on this consideration, complex electric amplitudes u_ℓ are decomposed as

$$u_\ell(\tau, \xi) = \mathcal{F}_\ell \exp i\varphi_\ell, \qquad (10)$$

where the φ_ℓ are temporal phases of the individual modes. Moreover, although the $\mathcal{F}_\ell$ are only determined by peak power and pulse width of each mode, the resulting φ_ℓ are slightly more complicated to compute and spell out as

$$\varphi_\ell = \varphi_{0\ell} - \Omega_\ell(\tau - \tau_{c\ell}) - \frac{C_\ell(\tau - \tau_{c\ell})^2}{2\sigma_\ell^2}, \qquad (11)$$

where $\varphi_{0\ell}$ is the respective initial phases. For simplicity, all of the latter are set to zero. Moreover, Ω_ℓ are frequency shifts, C_ℓ are chirp coefficients, and σ_ℓ are the root-mean-square (rms) pulse widths. The first-order derivatives for ξ with respect to the latter three variables have been derived by the moment method. Finally, we substitute the expanded complex functions u into Eqs. (7)–(9), yielding

$$\frac{dE_1}{d\xi} = \int_{-\infty}^{\infty} (2\varepsilon_{12} + \varepsilon_{13})d\tau, \qquad (12a)$$

$$\frac{dE_2}{d\xi} = \int_{-\infty}^{\infty} \left(-2\varepsilon_{12} + \frac{1}{2}\varepsilon_{23}\right)d\tau, \qquad (12b)$$

$$\frac{dE_3}{d\xi} = -\int_{-\infty}^{\infty} \left(\varepsilon_{13} + \frac{1}{2}\varepsilon_{23}\right)d\tau, \qquad (12c)$$

where ε_{12}, ε_{13}, and ε_{23} are nonlinear coupling variables written as

$$\varepsilon_{12} = \kappa_{12}\mathcal{F}_1(\tau - \tau_{c1})\mathcal{F}_2(\tau - \tau_{c2})\sin(\Delta\varphi_{12}), \qquad (13a)$$

$$\varepsilon_{13} = \kappa_{13}\mathcal{F}_1(\tau - \tau_{c1})\mathcal{F}_3(\tau - \tau_{c3})\sin(\Delta\varphi_{13}), \qquad (13b)$$

$$\varepsilon_{23} = \kappa_{23}\mathcal{F}_2(\tau - \tau_{c2})\mathcal{F}_3(\tau - \tau_{c3})\sin(\Delta\varphi_{23}), \qquad (13c)$$

and $\Delta\varphi_{12} = \varphi_1 - \varphi_2$, $\Delta\varphi_{13} = \varphi_1 - \varphi_3$, and $\Delta\varphi_{23} = \varphi_2 - \varphi_3$ are phase differences between the individual modes, $\kappa_{12} = \mathcal{R} \otimes (\mathcal{F}_1\mathcal{F}_2\cos\Delta\varphi_{12})$, $\kappa_{13} = \mathcal{R} \otimes (\mathcal{F}_1\mathcal{F}_3\cos\Delta\varphi_{13})$, and $\kappa_{23} = \mathcal{R} \otimes (\mathcal{F}_2\mathcal{F}_3\cos\Delta\varphi_{23})$ are convolution variables as a function of time. From Eqs. (12a) to (12c), we immediately see that the sign of energy derivative depends on the integral over ε, which relates back to $\Delta\varphi$. As an example, $\Delta\varphi_{12}$ can be written as

$$\Delta\varphi_{12} = \Omega_2(\tau - \tau_{c2}) - \Omega_1(\tau - \tau_{c1})$$
$$+ \frac{C_2(\tau - \tau_{c2})^2}{2\sigma_2^2} - \frac{C_1(\tau - \tau_{c1})^2}{2\sigma_1^2}. \qquad (14)$$

Equation (14) indicates that $\Delta\varphi_{12}$ relies on a multitude of effects, including frequency shift, temporal shift, chirp coefficient, and root-mean-square pulse width. Here, the temporal shift play an important role because they affect all four terms on the right-hand side of Eq. (14). We therefore conducted a series of numerical simulations by considering the four cases listed in Table II. With these simulations, we systematically explore the role of phase mismatch effects and

TABLE II. Parameter sets used in individual simulation runs. d_{12}, phase mismatch (MM) between fundamental and second-order mode. d_{13}, same but for third-order mode. T, response time of noninstantaneous Kerr medium (NKM).

	d_{12}	d_{13}	T	Comment
(i)	1	3	10	Strong MM, fast NKM
(ii)	1	3	100	Strong MM, slow NKM
(iii)	0.1	0.3	10	Weak MM, fast NKM
(iv)	0.1	0.3	100	Weak MM, slow NKM

walk-off on the one hand and that of the response time on the other hand. Moreover, the ratio between d_{12} and d_{13} was chosen as 1:3 as this was similar to what we expect in common multimode fibers. According to these calculations, we further chose $d_{22} = -1.1$ and $d_{23} = -1.2$, which are close but not identical to d_{21}.

III. SIMULATION RESULTS

We start our discussion of the simulation results with an analysis of the energy transfer between the individual modes; see Fig. 1. To this end, we depict the energy loss or gain $dE/d\xi$ in the first row of Fig. 1 as well as the energy E_i in the second one. The four cases in Table II are shown in columns (i) to (iv) of Fig. 1. We seed the computation by assuming identical energies in all three modes. In all our computations, the energy in the fundamental mode tends to grow at the expense of the higher-order modes. This effect is well known as self-cleaning [7] and is most pronounced for case (iii), i.e., weak intermode walk-off and a fast nonlinearity, and it is weakest for case (ii) with exactly opposite choice of parameters. In the latter case, group velocity differences as well as the response time are an order of magnitude larger than those in other three cases discussed. Therefore, case (ii) gives rise to a prominent walk-off effect between the three modes, effectively hampering energy exchange between the modes. In the other cases, time constants of this energy transfer between modes is mostly determined by the strength of the mismatch and shows surprisingly little influence on the relaxation time constant of the nonlinearity.

Apart from the energy transfer, temporal shifts are another aspect that we are interested in. The amount of temporal shift can be deduced from the position of pulse center, which is written as

$$\tau_{c\ell} = \frac{\int_{-\infty}^{\infty} \tau |u_\ell|^2 d\tau}{E_\ell}. \qquad (15)$$

Substituting Eqs. (1) and (4) into Eq. (15), and then using the overlap integrals provided in Table I, we finally reach

$$\frac{d\tau_{c1}}{d\xi} = d_{11} + d_{21}\Omega_1 + \frac{1}{E_1}\int_{-\infty}^{\infty}\left(2\rho_{12}^{M1} + \rho_{13}^{M1}\right)d\tau, \quad (16a)$$

$$\frac{d\tau_{c2}}{d\xi} = d_{12} + d_{22}\Omega_2 - \frac{2}{E_2}\int_{-\infty}^{\infty}\left(\rho_{12}^{M2} - \frac{1}{4}\rho_{23}^{M2}\right)d\tau, \quad (16b)$$

$$\frac{d\tau_{c3}}{d\xi} = d_{13} + d_{23}\Omega_3 - \frac{1}{E_3}\int_{-\infty}^{\infty}\left(\rho_{13}^{M3} + \frac{1}{2}\rho_{23}^{M3}\right)d\tau, \quad (16c)$$
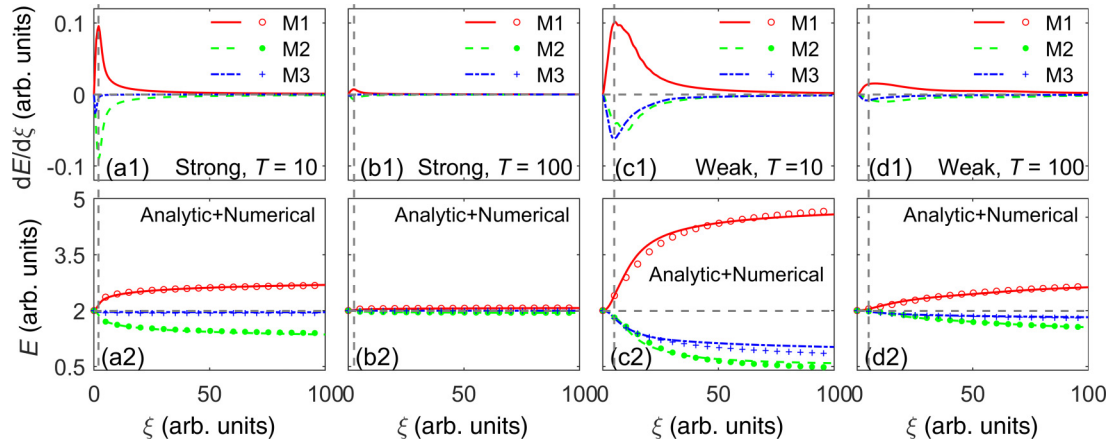
FIG. 1. Variations of energy derivative [top row (a1)–(d1)] and energy [bottom row (a2)–(d2)] with propagation distance ξ. Columns (a)–(d) refer to cases (i)–(iv) in Table II. Red solid, green dashed, and blue dash-dotted curves represent M1, M2, and M3, respectively. In the bottom row, curves represent analytic results. Hollow circle, solid circle, and plus sign represent numerical results for M1, M2, and M3, respectively.

where the six nonlinear coupling variables are given by $\rho_{jk}^{M\ell} = (\tau - \tau_{c\ell})\varepsilon_{jk}$. From Eqs. (16a) to (16c), one can see that the pulse center is affected by both linear and nonlinear parts. Considering $d\tau_{c1}/d\xi$, for example, the linear part is composed of two terms, namely d_{11} and $d_{21}\Omega_1$. Among these two terms, only the latter one marginally influences the temporal shift because of the small d_{21}; the linear contribution mostly stems from d_{11}. The integral term in Eqs. (16a) to (16c) describes nonlinear contributions to the timing between the modes. In order to understand the resulting timing behavior, we analytically evaluate the cases of strong and weak walk-off as illustrated in Fig. 2. For the case of strong walk-off, Figs. 2(a) and 2(b) show the evolution of ρ and τ_c, respectively, while Figs. 2(c) and 2(d) show the behavior for weak

FIG. 2. Variations of nonlinear coupling variable ρ and pulse center τ_c upon propagation along $\xi = z/L_D$ for modes M1, M2, and M3. (a) ρ under strong walk-off (top, M1; middle, M2; and bottom, M3). (b) τ_c, strong walk-off (top, M1; middle, M2; and bottom, M3). (c) ρ, weak walk-off. (d) τ_c, weak walk-off. In panels (b) and (d), red solid (M1), green dashed (M2), and blue dash-dotted (M3) curves represent analytic results while red hollow circle (M1), green solid circle (M2), and blue plus sign (M3) represent numerical results.

walk-off. As can be seen from Figs. 2(a) and 2(c), nonlinear coupling terms ρ_{12}^{M1} and ρ_{12}^{M2} strongly dominate the dynamics; i.e., there is predominant interaction between the fundamental and the second mode. For the case of weak walk-off, there also appears some sizable coupling between fundamental and third modes, whereas coupling between the second and third modes is always rather weak. Looking at the dominant coupling terms ρ_{12}^{M1} and ρ_{12}^{M2}, one observes an initial short phase of strongly correlated behavior, which only lasts for a few dispersion lengths for the strong walk-off scenario. In some sense of speaking, the interaction between the modes switches from predominantly nonlinear to linear, and this effect appears most pronounced for interaction involving M3. For the opposite case of weak walk-off, the correlation persists for about 15 L_D, which is seen to result in some synchronization between M1 and M2 in Fig. 2(d). Subsequently, the correlation vanishes, with damped oscillations of ρ_{12}^{M1} and ρ_{12}^{M2} at a relative phase difference of $\pi/2$. For the case of weak nonlinear coupling [Fig. 2(b)], the modes propagate close to their linear group velocity. While M3 propagates at the lowest speed, M1 is also slightly decelerated due to nonlinear interaction. In the case of strong nonlinear interaction in Fig. 2(d), M1 propagates the slowest whereas M2 and M3 are accelerated relative to their linear group velocity. Compared to Fig. 2(b), the temporal spread of the pulse centers remains about a factor 4 smaller, and we will see in the following that these small shifts appear due to a reshaping of the pulses in the individual modes rather than the intermodal dispersion of group velocity. The observed acceleration contrasts with the single-mode case [22,25], where only pulse deceleration was observed. While the nonlinear part also plays a negative role in $d\tau_{c3}/d\xi$, the amplitude of ρ for M3 is smaller due to the larger d_{23}. As a consequence, the linear part dominates $d\tau_{c3}/d\xi$ and the temporal pulse is thus delayed. The excellent fit between analytic and numerical results in Figs. 2(c) and 2(d) proves the validity of our theory. Additional simulations show that the spectra of all modes shift to the red. M1 generally shows the largest spectral shift and M3 the smallest when walk-off is strong. For weak walk-off, M2 and M3 red shift only during initial propagation and subsequently start to blue shift again. In the
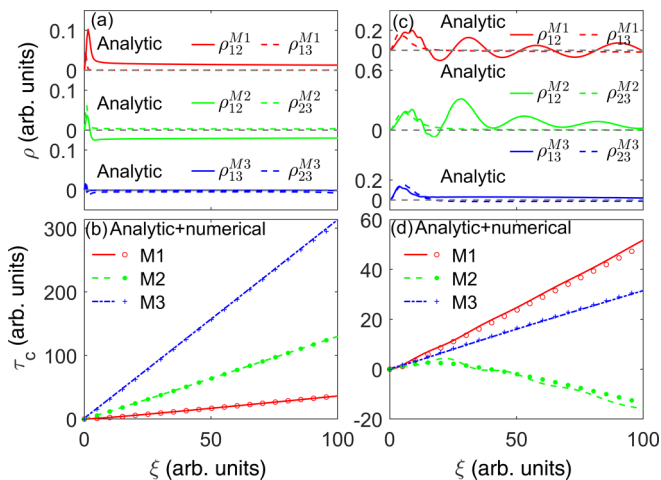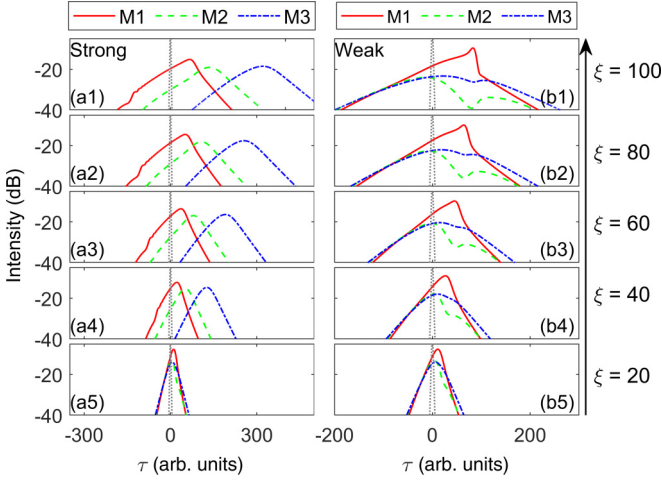
FIG. 3. Pulse shaping effects in the time domain. Left column (a1)–(a5), strong walk-off for $\xi = z/L_D$ 20 to 100, respectively. Right column (b1)–(b5), same for weak walk-off. Red solid, green dashed, and blue dash-dotted curves represent M1, M2, and M3, respectively.

latter case, red components of M2 and M3 are transferred into M1, and only blue components remain during subsequent propagation.

To further elucidate the dynamics of soliton acceleration, temporal wave forms under strong and weak walk-off are plotted at $T = 10$ for a range of propagation lengths in Fig. 3. The left columns (a1) to (a5) in Fig. 3 represent the wave forms under strong walk-off whereas the right columns (b1) to (b5) in Fig. 3 depict the case of weak walk-off. In the former case, M2 and M3 gradually fall behind M1, and all pulses are broadened mostly due to group-velocity dispersion. The leading edge of M1 is prolonged, which is a characteristic soliton feature in the presence of noninstantaneous Kerr nonlinearity [25]. Wave forms of all modes show smooth profiles due to the weak intermodal nonlinear interaction, and the temporal overlap of the individual modes remains nearly constant from $\xi = 40$ to 100, which explains the constant ρ_{12}^{M1} and ρ_{12}^{M2} in this range [Fig. 2(a)]. In contrast, when walk-off effects are weak [Fig. 3(b)], M1 travels at the nearly the same speed as M2 and M3, which leads to near- perfect temporal overlap during the entire propagation. In such a situation, pulse reshaping effects due to intermodal nonlinear coupling become unavoidable. Reshaping appears most prominently due to the energy transfer from M2 to the fundamental mode in a zone that travels from $\tau \approx 20$ at $z = 20L_D$ to 80 at $z = 100L_D$. This transfer decelerates the center of gravity of the pulse in the fundamental mode and splits the M2 pulse into two. The stronger leading pulse therefore appears accelerated relative to the propagation under strong walk-off in Fig. 3(a). A similar yet weaker effect can also be seen for M3 and explains the observed acceleration effects in Fig. 2(d).

IV. HYBRID NONINSTANTANEOUS KERR NONLINEARITY

In optical materials with NKM, one always finds an instantaneous optical Kerr nonlinearity that is typically caused by the polarization of bound electrons [44]. Even for the

case of liquid CS_2 with its massive noninstantaneous response due to molecular reorientation, a concomitant instantaneous response has been reported [25]. On the other hand, the instantaneous Kerr effect in optical glasses or crystalline materials is also often accompanied by a Raman response, which can be understood as a NKM, too. The ratio between the two types of responses depends on the optical materials and underlying physical mechanisms [30,45,46]. To include both nonlinearities in our model, Eq. (1) is modified by introducing a fractional variable f_r, which describes the proportion of the noninstantaneous Kerr nonlinearity. This hybrid multimode GNLSE is written as

$$\frac{\partial u_p}{\partial \xi} = i d_{0p} u_p - d_{1p} \frac{\partial u_p}{\partial \tau} - i \frac{d_{2p}}{2} \frac{\partial^2 u_p}{\partial \tau^2} + i N_s^2 \sum_{lmnp} f_{lmnp}$$

$$\times \{(1 - f_r) u_\ell u_m u_n^* + f_r u_\ell [\mathcal{R} \otimes u_m u_n^*]\}, \quad (17)$$

where d_{0p} is the same as in Eq. (1), and $(1 - f_r)$ is the proportion of the instantaneous Kerr nonlinearity. It should be noted that Eq. (17) strictly only holds for linear polarization, but can be adapted to the case of circular polarization by inserting an additional factor 2/3 in front of the $(1 - f_r)$ term [35]. Depending on their degeneracy, the $u_l u_m u_n^*$ in Eq. (17) models the entire suite of four-wave mixing processes including SPM, XPM, as well as degenerate FWM effects between the three modes. Adopting the same procedure as in the above section, energy derivatives for M1, M2, and M3 are written as

$$\frac{dE_1}{d\xi} = \int_{-\infty}^{\infty} (2\chi_{12} + \chi_{13}) d\tau, \quad (18a)$$

$$\frac{dE_2}{d\xi} = -\int_{-\infty}^{\infty} \left(2\chi_{12} - \frac{1}{2}\chi_{23}\right) d\tau, \quad (18b)$$

$$\frac{dE_3}{d\xi} = -\int_{-\infty}^{\infty} \left(\chi_{13} + \frac{1}{2}\chi_{23}\right) d\tau, \quad (18c)$$

where χ_{12}, χ_{13}, and χ_{23} are intermodal nonlinear coupling variables for hybrid NKM. These variables can be expanded to

$$\chi_{12} = (1 - f_r)\varepsilon_{12}^K + f_r \varepsilon_{12}, \quad (19a)$$

$$\chi_{13} = (1 - f_r)\varepsilon_{13}^K + f_r \varepsilon_{13}, \quad (19b)$$

$$\chi_{23} = (1 - f_r)\varepsilon_{23}^K + f_r \varepsilon_{23}, \quad (19c)$$

where the $\varepsilon_{\ell m}^K$ are similar to the $\varepsilon_{\ell m}$ for the case of pure NKM. These newly introduced variables spell out as

$$\varepsilon_{12}^K = \frac{1}{2}\mathcal{F}_1^2(\tau - \tau_{c1})\mathcal{F}_2^2(\tau - \tau_{c2})\sin(2\Delta\varphi_{12}), \quad (20a)$$

$$\varepsilon_{13}^K = \frac{1}{2}\mathcal{F}_1^2(\tau - \tau_{c1})\mathcal{F}_3^2(\tau - \tau_{c3})\sin(2\Delta\varphi_{13}), \quad (20b)$$

$$\varepsilon_{23}^K = \frac{1}{2}\mathcal{F}_2^2(\tau - \tau_{c2})\mathcal{F}_3^2(\tau - \tau_{c3})\sin(2\Delta\varphi_{23}). \quad (20c)$$

Unlike pure NKM, the above three equations do not require convolutions as they only take into account the instantaneous Kerr effect. Since $\int_{-\infty}^{\infty} \mathcal{R} d\tau = 1$ and $\mathcal{F}_\ell \leqslant 1$ holds, we conclude that $\varepsilon_{jk} \leqslant \varepsilon_{jk}^K$; that is, the Kerr nonlinearity serves to further enhance the magnitude of the nonlinear coupling variables χ defined in Eqs. (19a)–(19c).
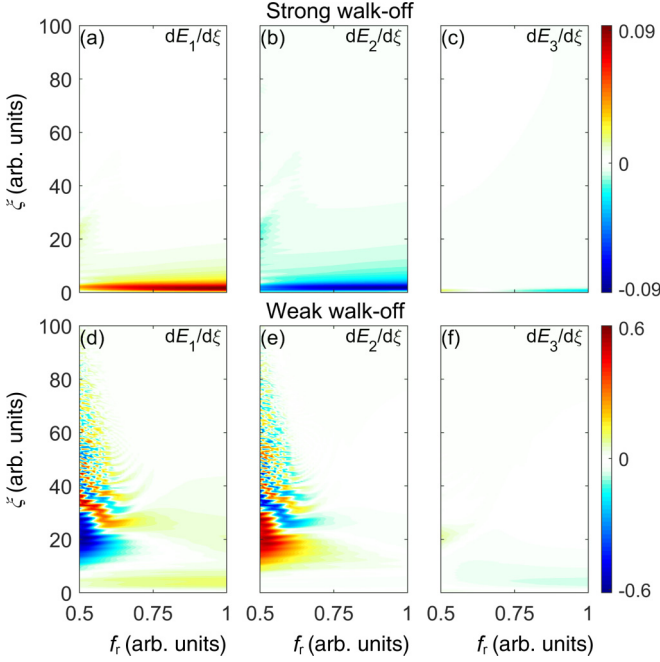
FIG. 4. Evolutions of energy derivatives along propagation with fast nonlinearity ($T = 10$). Top panel, strong walk-off. (a) M1, (b) M2, and (c) M3. Bottom panel, weak walk-off. (d) M1, (e) M2, and (f) M3. Note that energy derivatives in the top three panels are more than 10 times smaller than in the bottom ones. All energy derivatives are with arbitrary units.
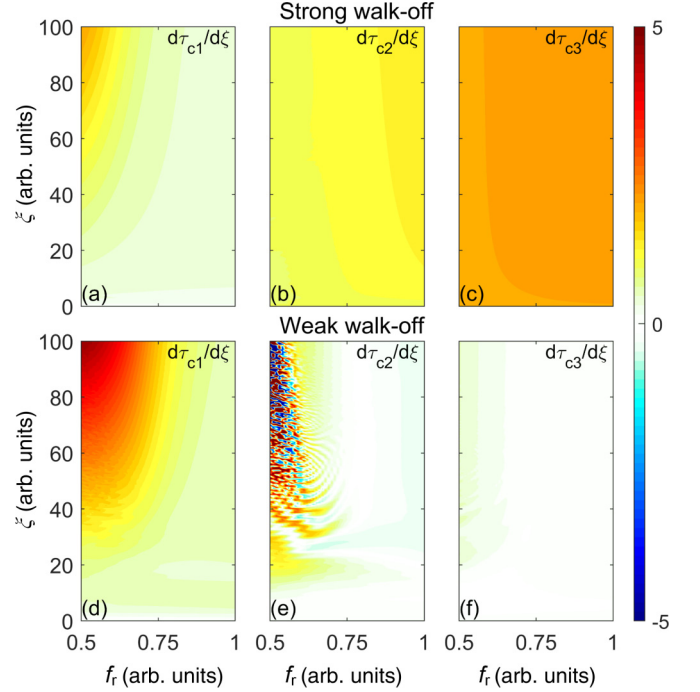

FIG. 5. Evolutions of derivatives of pulse centers. All other parameters and panel layout identical to Fig. 4. All derivatives of pulse centers are with arbitrary units.

To verify our expectations, we numerically solve Eqs. (18a)–(18c), varying the NKM ratio f_r from 0.5 to 1 and fixing $T = 10$. The simulation results are shown in Fig. 4, again with the top and bottom three panels discussing the case of strong and weak walk-off, respectively. In these panels, we depict the derivatives $dE_m/d\xi$; i.e., an energy gain of the respective mode is shown in yellow to red colors, and losses are indicated by blue shades. For the case of strong walk-off [Figs. 4(a)–4(c)], an energy exchange between the modes virtually only appears in an initial stage of propagation $z < 10L_\mathrm{D}$. In the absence of an instantaneous contribution ($f_r = 1$), one observe a rapid energy equilibration between the modes as already discussed in Fig. 1(a1). In this process, the fundamental mode gains energy mostly at the expense of M2. Transfer of energy from M3 plays a much lesser role and is limited to an even earlier phase of the propagation. After the energy flow reached its maximum at $z \approx 3L_\mathrm{D}$, the exchange steadily decreases until an equilibrium state is reached. The dynamics of this process depends only weakly on f_r, with a tendency of a reduced energy exchange in the presence of a strong instantaneous nonlinearity ($f_r = 0.5$). Moreover, in the latter situation, one can also observe a periodic energy exchange between M1 and M2 with a period of $\approx 2.5L_\mathrm{D}$. This tendency of relaxation-oscillation like equilibration strongly increases for weak walk-off [Figs. 4(d)–4(f)] and $f_r \leqslant 0.7$. In this case, one can actually see an additional slower oscillation frequency, which increases upon further propagation along z. For the weak walk-off scenario, the relaxation oscillation behavior clearly dominates in the presence of a sizable instantaneous nonlinearity. While the relaxation oscillation behavior is initially triggered by the weak walk-off, Eqs. (19a)–(19c) take over for propagation beyond $z = 10L_\mathrm{D}$ until an equilibrium state is eventually reached at $z > 80L_\mathrm{D}$.

For the temporal shift in hybrid NKM, expressions similar to Eqs. (16a), (16b), and (16c) can be derived:

$$\frac{d\tau_{c1}}{d\xi} = d_{11} + d_{21}\Omega_1 + \frac{1}{E_1}\int_{-\infty}^{\infty}\left(2\chi_{12}^{M1} + \chi_{13}^{M1}\right)d\tau, \quad (21a)$$

$$\frac{d\tau_{c2}}{d\xi} = d_{12} + d_{22}\Omega_2 - \frac{2}{E_2}\int_{-\infty}^{\infty}\left(\chi_{12}^{M2} - \frac{1}{4}\chi_{23}^{M2}\right)d\tau, \quad (21b)$$

$$\frac{d\tau_{c3}}{d\xi} = d_{13} + d_{23}\Omega_3 - \frac{1}{E_3}\int_{-\infty}^{\infty}\left(\chi_{13}^{M3} + \frac{1}{2}\chi_{23}^{M3}\right)d\tau, \quad (21c)$$

where $\chi_{jk}^{M\ell} = (\tau - \tau_{c\ell})\chi_{jk}$. One can see that $d\tau_{c\ell}/d\xi$ are again composed of linear and nonlinear parts for hybrid NKM. However, the nonlinear part is more involved than in pure NKM, given the participation of the instantaneous Kerr nonlinearity. Therefore, we now resort to numerical simulations. Pertinent simulation results of the derivatives of pulse center positions $d\tau_{c\ell}/d\xi$ are shown in Fig. 5. Acceleration is shown in blue shades whereas deceleration is depicted in yellow to red hues. Again, for the case of vanishing instantaneous contributions to the nonlinearity ($f_r = 1$), one can compare Figs. 5(a)–5(c) to Fig. 2(b); i.e., the three modes propagate essentially linearly after a short phase of nonlinear interaction ($z < 20L_\mathrm{D}$). Reducing f_r, i.e., increasing the instantaneous contribution, an additional acceleration sets in for M1, whereas M2 and M3 remain mostly unaffected but for a general slight reduction of the overall acceleration due to the nonlinearity. For weak walk-off [Figs. 5(d)–5(f)], tendencies are similar, but rather strong acceleration and deceleration effects appear with a strong influence of instantaneous effects
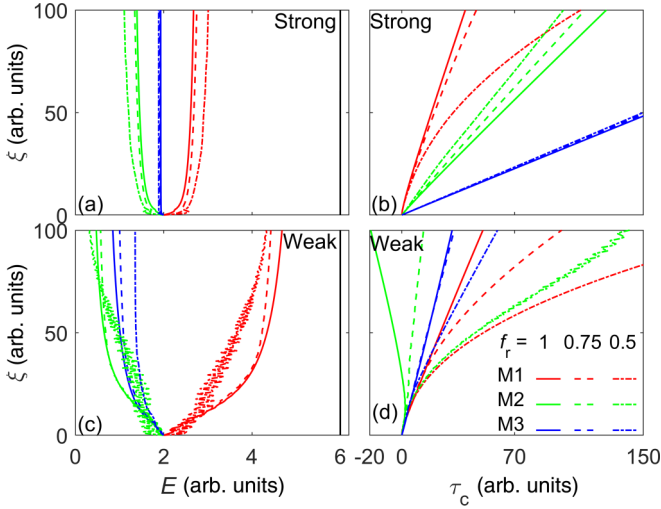
FIG. 6. Evolutions of (a) energy and (b) pulse center under strong walk-off. Evolutions of (c) energy and (d) pulse center under weak walk-off with fast nonlinearity ($T = 10$). Red (green, blue) solid, red (green, blue) dashed, and red (green, blue) dash-dotted curves represent $f_r = 1$, 0.75 and 0.5 for M1 (M2, M3), respectively.

as a consequence of the previously discussed relaxation oscillations. In addition to the color map representations of energy transfer and timing (Figs. 4 and 5, respectively), we additionally plotted the evolution of modal energies E_j and timing τ_{cj} as a function of normalized propagation distance ξ for three exemplary values of $f_r \in \{0.5, 0.75, 1\}$; see Fig. 6. For the case of vanishing instantaneous contributions $f_r = 1$, the solid lines in Figs. 6(a) and 6(c) correspond to the cases already discussed in Figs. 1(a2) and 1(c2), respectively. Comparing the dashed ($f_r = 0.75$) and dash-dotted ($f_r = 0.5$) lines for the case of strong coupling in Fig. 6(a), one can generally see that the instantaneous nonlinearity further increase the energy transfer from M2 into M1. The situation is more complicated for weak walk-off [Fig. 6(b)], but markedly only affects the extreme case of $f_r = 0.5$, which is again explained by the previously discussed relaxation oscillations. The timing of the pulse center is depicted in Figs. 6(b) and 6(d). Again, the solid lines in the latter plots correspond to Figs. 2(b) and 2(d), respectively. For strong walk-off, the pulse trajectories are essentially straight lines, and the fundamental mode is accelerated with increasing instantaneous contribution to the nonlinearity whereas M2 experiences the opposite effect. For $f_r = 0.5$, one can see an additional accelerating effect during propagation; i.e., the trajectory becomes curved. The additional acceleration then stagnates for large values of z. Subsequently, the pulse in the fundamental mode propagates with constant velocity. This curving effect appears to be similar in nature as previously reported interactions between solitons and dispersive waves in the so-called event horizon scenario in single-mode fibers [47]. For weak walk-off, the tendency for trajectory curving further increases and also heavily affects M2 [Fig. 6(d)]. In all these dynamics, M3 appears widely unaffected, as the predominant energy exchange is always between M1 and M2. Moreover, relaxation oscillations only appear to marginally affect the timing of the pulses, giving rise to some rather faint oscillations of τ_{c2} in

Fig. 6(d). When f_r is decreased from 1 to 0.75 and 0.5, the amount of red shift is increased for M1, regardless of the walk-off. For M2, the amount of red shift decreases with decreasing f_r if the walk-off is strong. However, when walk-off is weak, M2 initially blue shifts but then shifts to the red at decreased f_r. For M3, the red shift remains almost unchanged for strong walk-off, regardless of variation of f_r. In contrast, the amount of red shift is increased with decreased f_r for weak walk-off. As the reason for this somewhat nonuniform behavior, we find that a decreased f_r generally enhances energy transfer from M2 and M3 to M1.

V. VARYING NONINSTANTANEOUS KERR NONLINEARITY

Some recent studies suggest that the nonlinear refractive index n_2 of the NKM may change with pulse width during propagation [20,48]. For short pulses in the femtosecond range, bound electrons contribute significantly to n_2, leading to an instantaneous nonlinear response. For longer pulse in the picosecond range, n_2 may be dominated by noninstantaneous nuclear nonlinearities, such as molecule libration and reorientation. Following this model assumption for the pulse between 100 fs and 1 ps, n_2 is then composed of both an instantaneous and a noninstantaneous Kerr nonlinearity. Accordingly, n_2 is now written as [20]

$$n_2 = n_{2e} + \frac{\int_{-\infty}^{\infty} I(\tau)[\mathcal{R} \otimes I(\tau)]d\tau}{\int_{-\infty}^{\infty} I^2(\tau)d\tau}, \qquad (22)$$

where n_{2e} denotes the constant instantaneous nonlinearity. The second term on the right-hand side represents the noninstantaneous Kerr nonlinearity, which changes with pulse width and is referred to as n_{2m}. f_r is now defined as $f_r(\xi) = n_{2m}(\xi)/n_2(\xi)$ in the context of varying NKM. For varying NKM, f_r is not assumed constant but may vary upon propagation. Consequently, we have to modify Eq. (17) for describing the varying noninstantaneous Kerr nonlinearity by adding an extra $n_2(\xi)$,

$$\frac{\partial u_p}{\partial \xi} = id_{0p}u_p - d_{1p}\frac{\partial u_p}{\partial \tau} - i\frac{d_{2p}}{2}\frac{\partial^2 u_p}{\partial \tau^2} + iN_s^2 n_2(\xi)$$

$$\times \sum_{lmnp} f_{\ell mnp}\{(1 - f_r)u_\ell u_m u_n^* + f_r u_\ell[\mathcal{R} \otimes u_m u_n^*]\}.$$

$$(23)$$

Here, the value of $n_{2m}(\xi)$ at $\xi = 0$ is calculated as 1.2 according to Eq. (22), and we therefore let $n_{2e}(\xi = 0) = 0.2n_{2m}(\xi = 0)$. The corresponding f_r is calculated as 0.83, which is close to the value of 0.85 that was assumed in Ref. [25]. In order to solve Eq. (23), $n_2(\xi)$ is normalized to $n_2(\xi = 0)$. Simulation results are shown in Fig. 7, where τ_F denotes the full width at half maximum. As we want to approach the problem from a practical perspective, we have based the calculation of τ_F on the assumption that the temporal pulse in the three modes can be regarded as an entirety during propagation. Moreover, the response time T may affect τ_F in the varying NKM scenario. We therefore consider the two cases of $T = 10$ and 100 for comparison. While Fig. 7 shows some quantitative differences for the the evolution of τ_F, of the effective nonlinearity n_2, and
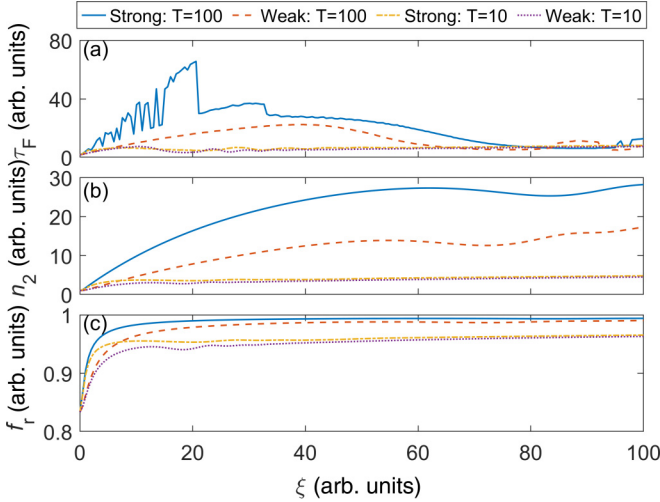
FIG. 7. Evolutions of (a) pulse width, (b) nonlinear refractive index, and (c) f_r along propagation. Blue solid, red dashed, yellow dash-dotted, and violet dotted curves represent strong walk-off with $T = 10$, strong walk-off with $T = 100$, weak walk-off with $T = 10$, and weak walk-off with $T = 100$, respectively

of f_r, there is nevertheless a common trend independent of T, and the strength of walk-off effects. Starting with $\tau_F = 1$, the pulse duration initially increases, which is accompanied by an increase of n_2 and f_r. Due to the steadily increasing pulse duration, the noninstantaneous contributions to the nonlinearity become more effective and may increase by more of an order of magnitude for $T = 100$. In this process, we observe a transition from a typical hybrid nonlinearity to a nearly pure NKM. The resulting effective growth of the nonlinearity also effects the nonlinear coupling, and, in turn, further pulse spreading is prevented and the pulse eventually even recompresses to shorter pulse duration. At the end of this process, a balance is found at $\tau_F \approx 5$; i.e., a fairly stable spatiotemporal wave packet has formed. Here the final pulse duration is only marginally affected by the choice of T as long as $T \gg \tau_F$, but the stability of the wave packet appears to be strongly affected by T.

For a more quantitative analysis on how the varying n_2 and f_r influence energy transfer and temporal shifts, we numerically solve Eq. (23) together with Eq. (22). For comparison two cases of a constant f_r are considered, namely $f_r = 1$ and 0.83 are considered. Simulation results for M1 are listed in Table III. Here E_1 and τ_{c1} are resulting output energy and nonlinearly induced temporal shift of M1 after propagation to $\xi = 100$, respectively. For varying f_r, one can easily see that E_1 and τ_{c1} are maximized, no matter whether strong or weak walk-off. This enhancement can be attributed to the increased effective n_2 during propagation, similar to what we already discussed in Fig. 7. We therefore find that both walk-off and Kerr nonlinearity affect the energy transfer and temporal shifts, effectively enhancing intermodal nonlinear coupling via the convolution integrals in Eq. (23). For varying NKM, the convolution integrals only start to kick in once the pulse has sufficiently lengthened and the n_2 nonlinearity is effectively increased. To further unveil the role of a varying n_2 in intermodal nonlinear interaction, we analyze the

TABLE III. Comparisons of E_1 and τ_{c1} for different types of nonlinearity and different time constants T of the noninstantaneous nonlinearity. $f_r = 1$ corresponds to a pure noninstantaneous nonlinearity and $f_r = 0.83$ to a constant addition of a instantaneous contribution. The varying case assumes a pulse-width-dependent nonlinearity according to Eq. (23).

		Strong walk-off			Weak walk-off		
	f_r	1	0.83	Varying	1	0.83	Varying
E_1	$T = 100$	2.07	2.22	2.70	2.65	2.79	4.79
	$T = 10$	2.68	2.71	3.67	4.68	4.58	5.70
τ_{c1}	$T = 100$	5.44	9.83	60.15	10.01	11.39	53.59
	$T = 10$	39.41	42.04	174.40	50.07	67.55	178.50

accumulated nonlinear phase φ_N, which is also known as the "B integral." Here we define

$$\varphi_\ell(\xi) = \int_0^\xi n_2(\xi') P_\ell(\xi') d\xi', \qquad (24)$$

where $P_\ell(\xi)$ is the peak power in mode Mℓ. Numerically solving Eqs. (23) and (24), evolutions of φ_ℓ along propagation for the three modes are shown in Fig. 8. Here it is striking that nonlinear phase accumulation nearly exclusively affects M1, which further seems to be rather independent of strong or weak walk-off. However, the B integral doubles when the time constant T increases by an order of magnitude. Moreover, the effect on the higher order modes is weakest for weak walk-off and low values of T and strongest for the opposite scenario. Finally, to shed more light on the influence of varying n_2, both temporal and spectral characteristics of output pulse after $\xi = 100$ are analyzed using cross-correlation frequency-resolved optical gating (XFROG) spectrograms, as was commonly used to explore the dynamics of nonlinear propagation in single-mode fibers [49,50]. To this end, we
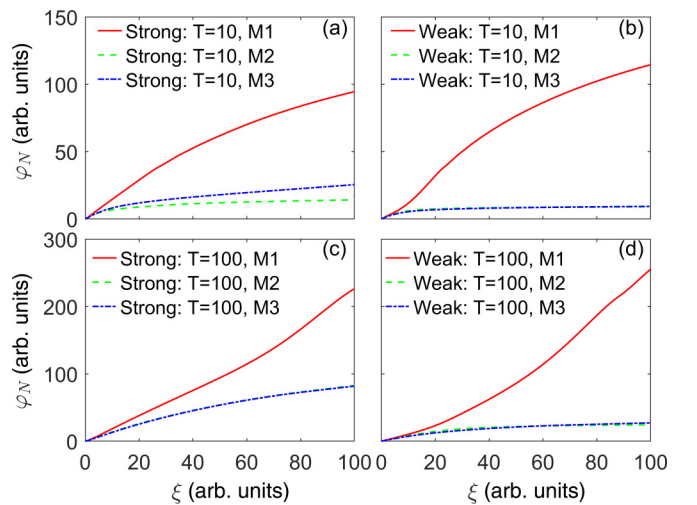

FIG. 8. Nonlinear phases of M1, M2, and M3 when (a) walk-off is strong and $T = 10$; (b) walk-off is weak and $T = 10$; (c) walk-off is strong and $T = 100$; and (d) walk-off is weak and $T = 100$. Red solid, green dashed, and blue dash-dotted curves represent M1, M2, and M3, respectively.
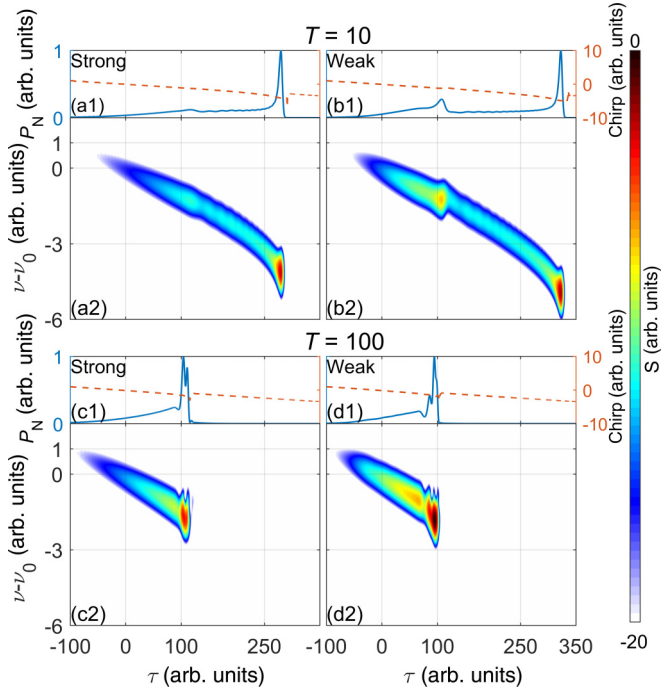
FIG. 9. Temporal waveforms (blue solid curves) and chirp (red dashed curves) under (a1) strong walk-off and $T = 10$, (a2) weak walk-off and $T = 10$, (a3) strong walk-off and $T = 10$, and (a4) weak walk-off, $T = 100$; (a2), (b2), (c2), and (d2) are corresponding XFROG spectrograms.

define the XFROG trace

$$S(\tau', \omega) = \left| \int_{-\infty}^{\infty} u_{\text{out}}(\tau) G(\tau - \tau') \exp(i\omega\tau) d\tau \right|^2, \quad (25)$$

where τ' is a variable time delay. The gate pulse $G(\tau)$ is assumed to be Gaussian

$$G(\tau) = \exp\left[-\frac{\tau^2}{2\tau_0^2} \right]. \quad (26)$$

For practical purposes, we assumed $\tau_0 = 2$. Figure 9 depicts the emerging soliton dynamics for all combinations of slow and fast nonlinearity as well as strong and weak walk-off. The general behavior is similar in all cases. The soliton experiences a self-frequency shift due the noninstantaneous part of the nonlinearity toward lower frequencies. The further the soliton is shifted toward the infrared, the slower it propagates, which then also leads to an increased anomalous dispersion

at the shifted center wavelength. Adiabatic reshaping of the soliton causes some bleeding of energy into the temporal continuum, which leads to the formation of a comet-like trail advancing the soliton. When the nonlinearity is fast [Figs. 9(a) and 9(b)], dispersive effects cause a massive transfer of energy into the continuum, and a second soliton forms in the wake of the champion soliton. In the opposite case of a slow nonlinearity [Figs. 9(c) and 9(d)], both the energy loss and the self-frequency shift are mitigated. Pulse energy remains localized around the soliton. Yet, some early stage of a pulse breakup indicates that the temporal confinement will eventually break up upon further propagation.

VI. CONCLUSIONS

In this paper, intermodal synchronization effects of multimode soliton propagation in NKM are studied analytically and numerically. Unlike the behavior of single-mode solitons in NKM, both temporal acceleration and deceleration effects can be observed, leading to nonlinear coupling and formation of a temporal bond between different spatial modes during propagation. While these effects already appear in purely noninstantaneous nonlinearity, the additional presence of a Kerr nonlinearity can serve to further enhance this nonlinear coupling mechanism. This case appears particularly interesting, as the relative timing of solitons in different modes can be affected by the nonlinear coupling. Similar to the suggested switching schemes between dispersive wave and solitons, this interaction could be exploited for photonic switching schemes, with the additional advantage of avoiding excessive dispersive stretching. Other potential applications are an increased modal self-cleaning effect due to the noninstantaneous nonlinearity. Finally, these delayed nonlinearities also exhibit a remarkable potential for stabilizing a soliton against pulse breakup effects during the self-frequency shift. Practical implementations range from glasses with their pronounced Raman effect to hollow-core fibers that are filled with liquids [51] like CS_2. Compared with previous work on multimode in instantaneous Kerr media, our study on noninstantaneous nonlinearities therefore reveals a number of interesting findings and possibilities, which may open other directions in multimode nonlinear optics.

[1] A. Hasegawa, Self-confinement of multimode optical pulse in a glass fiber, Opt. Lett. **5**, 416 (1980).

[2] B. Crosignani and P. Di Porto, Soliton propagation in multimode optical fibers, Opt. Lett. **6**, 329 (1981).

[3] B. Crosignani, A. Cutolo, and P. Di Porto, Coupled-mode theory of nonlinear propagation in multimode and single-mode fibers: Envelope solitons and self-confinement, J. Opt. Soc. Am. **72**, 1136 (1982).

[4] W. H. Renninger and F. W. Wise, Optical solitons in graded-index multimode fibres, Nat. Commun. **4**, 1719 (2013).

[5] A. S. Ahsan and G. P. Agrawal, Graded-index solitons in multimode fibers, Opt. Lett. **43**, 3345 (2018).

[6] T. Hansson, A. Tonello, T. Mansuryan, F. Mangini, M. Zitelli, M. Ferraro, A. Niang, R. Crescenzi, S. Wabnitz, and V. Couderc, Nonlinear beam self-imaging and self-focusing dynamics in a grin multimode optical fiber: Theory and experiments, Opt. Express **28**, 24005 (2020).

[7] K. Krupa, A. Tonello, B. M. Shalaby, M. Fabert, A. Barthélémy, G. Millot, S. Wabnitz, and V. Couderc, Spatial beam self-cleaning in multimode fibres, Nat. Photon. **11**, 237 (2017).

[8] R. Guenard, K. Krupa, R. Dupiol, M. Fabert, A. Bendahmane, V. Kerméne, A. Desfarges-Berthelemot, J. L. Auguste, A. Tonello, A. Barthélémy, G. Millot, S. Wabnizt, and V. Couderc, Kerr self-cleaning of pulsed beam in an ytterbium doped multimode fiber, Opt. Express **25**, 4783 (2017).

[9] N. B. Terry, T. G. Alley, and T. H. Russell, An explanation of SRS beam cleanup in graded-index fibers and the absence of SRS beam cleanup in step-index fibers, Opt. Express **15**, 17509 (2007).

[10] Q. Gao, Z. Lu, C. Zhu, and J. Zhang, Mechanism of beam cleanup by stimulated Brillouin scattering in multimode fibers, Appl. Phys. Express **8**, 052501 (2015).

[11] A. Antikainen, L. Rishøj, B. Tai, S. Ramachandran, and G. P. Agrawal, Fate of a Soliton in a High Order Spatial Mode of a Multimode Fiber, Phys. Rev. Lett. **122**, 023901 (2019).

[12] P. Aschieri, J. Garnier, C. Michel, V. Doya, and A. Picozzi, Condensation and thermalization of classsical optical waves in a waveguide, Phys. Rev. A **83**, 033838 (2011).

[13] A. Fusaro, J. Garnier, K. Krupa, G. Millot, and A. Picozzi, Dramatic Acceleration of Wave Condensation Mediated by Disorder in Multimode Fibers, Phys. Rev. Lett. **122**, 123902 (2019).

[14] M. Zitelli, F. Mangini, M. Ferraro, A. Niang, D. Kharenko, and S. Wabnitz, High-energy soliton fission dynamics in multimode grin fiber, Opt. Express **28**, 20473 (2020).

[15] L. G. Wright, W. H. Renninger, D. N. Christodoulides, and F. W. Wise, Spatiotemporal dynamics of multimode optical solitons, Opt. Express **23**, 3492 (2015).

[16] S. Buch and G. P. Agrawal, Soliton stability and trapping in multimode fibers, Opt. Lett. **40**, 225 (2015).

[17] A. S. Ahsan and G. P. Agrawal, Spatio-temporal enhancement of Raman-induced frequency shifts in graded-index multimode fibers, Opt. Lett. **44**, 2637 (2019).

[18] M. F. Saleh, A. Armaroli, A. Marini, and F. Biancalana, Strong Raman-induced noninstantaneous soliton interactions in gas-filled photonic crystal fibers, Opt. Lett. **40**, 4058 (2015).

[19] R. V. J. Raja, A. Husakou, J. Hermann, and K. Porsezian, Supercontinuum generation in liquid-filled photonic crystal fiber with slow nonlinear response, J. Opt. Soc. Am. B **27**, 1763 (2010).

[20] M. Reichert, H. Hu, M. R. Ferdinandus, M. Seidel, P. Zhao, T. R. Ensley, D. Peceli, J. M. Reed, D. A. Fishman, S. Webster, D. J. Hagan, and E. W. Van Stryland, Temporal, spectral, and polarization dependence of the nonlinear optical response of carbon disulfide, Optica **1**, 436 (2014).

[21] C. Conti, M. A. Schmidt, P. St. J. Russell, and F. Biancalana, Highly Noninstantaneous Solitons in Liquid-Core Photonic Crystal Fibers, Phys. Rev. Lett. **105**, 263902 (2010).

[22] W. Hong, Q. Guo, and L. Li, Dynamics of optical pulses in highly noninstantaneous Kerr media, Phys. Rev. A **92**, 023803 (2015).

[23] F. Deng, W. Hong, and D. Deng, Airy-type solitary wave in highly noninstantaneous Kerr media, Opt. Express **24**, 15997 (2016).

[24] K. Yi, R. Chen, and W. Hong, Dynamics of Pearcey pulses in highly noninstantaneous Kerr media, Jpn. J. Appl. Phys. **59**, 032001 (2020).

[25] M. Chemnitz, M. Gebhardt, C. Gaida, F. Stutzki, J. Kobelke, J. Limpert, A. Tünnermann, and M. A. Schmidt, Hybrid soliton dynamics in liquid-core fibres, Nat. Commun. **8**, 42 (2017).

[26] M.-R. S. Tchio, S. Abdoulkary, and A. Mohamadou, Raman peak shifts due to walk-off in non-instantaneous Kerr media with higher-order effects, J. Opt. Soc. Am. B **36**, 3479 (2019).

[27] A. Canabarro, B. Santos, B. de Lima Bernardo, A. L. Moura, W. C. Soares, E. de Lima, I. Gléria, and M. L. Lyra, Modulation instability in noninstantaneous Kerr media with walk-off and cross-phase modulation for mixed group-velocity-dispersion regimes, Phys. Rev. A **93**, 023834 (2016).

[28] S. V. Palacio and R. A. Herrera, Dispersive wave and four-wave mixing generation in noninstantaneous nonlinear fiber solitons, Appl. Opt. **58**, 2736 (2019).

[29] S. Pricking and H. Giessen, Generalized retarded response of nonlinear media and its influence on soliton dynamics, Opt. Express **19**, 2895 (2011).

[30] M. Chemnitz, C. Gaida, M. Gebhardt, F. Stutzki, J. Kobelke, A. Tünnermann, J. Limpert, and M. A. Schmidt, Carbon chloride-core fibers for soliton mediated supercontinuum generation, Opt. Express **26**, 3221 (2018).

[31] J. Santhanam and G. P. Agrawal, Raman-induced spectral shifts in optical fibers: General theory based on the moment method, Opt. Commun. **222**, 413 (2003).

[32] H. Steffensen, C. Agger, and O. Bang, Influence of two-photon absorption on soliton self-frequency shift, J. Opt. Soc. Am. B **29**, 484 (2012).

[33] F. Poletti and P. Horak, Description of ultrashort pulse propagation in multimode optical fibers, J. Opt. Soc. Am. B **25**, 1645 (2008).

[34] A. Mafi, Pulse propagation in short nonlinear graded-index multimode optical fiber, J. Lightwave Technol. **30**, 2803 (2012).

[35] P. Horak and F. Poletti, Multimode nonlinear fibre optics: Theory and applications, in *Recent Progress in Optical Fiber Research*, edited by M. Yasin, S. W. Harun, and H. Arof (IntechOpen, Rijeka, 2012), Chap. 1.

[36] A. W. Snyder and J. D. Love, *Optical Waveguide Theory* (Chapman and Hall, London, 1983).

[37] F. Poletti and P. Horak, Dynamics of femtosecond supercontinuum generation in multimode fibers, Opt. Express **17**, 6134 (2009).

[38] S. Buch and G. P. Agrawal, Intermodal soliton interaction in nearly degenerate modes of a multimode fiber, J. Opt. Soc. Am. B **33**, 2217 (2016).

[39] L. Zhang, P. Huang, C. Conti, Z. Wang, Y. Hu, D. Lei, Y. Li, and D. Fan, Decelerating Airy pulse propagation in highly non-instantaneous cubic media, Opt. Express **25**, 1856 (2017).

[40] K. Krupa, A. Tonello, A. Barthélémy, T. Mansuryan, V. Couderc, G. Millot, P. Grelu, D. Modotto, S. A. Babin, and S. Wabnitz, Multimode nonlinear fiber optics, a spatiotemporal avenue, APL Photon. **4**, 110901 (2019).

[41] V. L. Kalashnikov and S. Wabnitz, Distributed Kerr-lens mode locking based on spatiotemporal dissipative solitons in multimode fiber lasers, Phys. Rev. A **102**, 023508 (2020).

[42] A. Picozzi, G. Millot, and S. Wabnitz, Nonlinear virtues of multimode fibre, Nat. Photon. **9**, 289 (2015).

[43] A. B. Grudinin, E. M. Dianov, D. V. Korbkin, A. M. Prokhorov, and D. Khadarov, Nonlinear mode coupling in multimode optical fibers; Excitation of femtosecond-range stimulated-Raman-scattering solitons, Sov. JETP Lett. **47**, 356 (1988).

[44] M. Sheik-Bahae, D. Hutchings, D. Hagan, and E. Van Stryland, Dispersion of bound electron nonlinear refraction in solids, IEEE J. Quantum Electron. **27**, 1296 (1991).

[45] J. J. Wathen, V. R. Pagan, R. J. Suess, K.-Y. Wang, A. C. Foster, and T. E. Murphy, Non-instantaneous optical nonlinearity of an a-Si:H nanowire waveguide, Opt. Express **22**, 22730 (2014).

[46] M. Hofmann, J. Hyyti, S. Birkholz, M. Bock, S. K. Das, R. Grunwald, M. Hoffmann, T. Nagy, A. Demircan, M. Jupé, D. Ristau, U. Morgner, C. Brée, M. Woerner, T. Elsaesser, and G. Steinmeyer, Noninstantaneous polarization dynamics in dielectric media, Optica **2**, 151 (2015).

[47] I. Babushkin, A. Tajalli, H. Sayinc, U. Morgner, G. Steinmeyer, and A. Demircan, Simple route toward efficient frequency conversion for generation of fully coherent supercontinua in the mid-IR and UV range, Light Sci. Appl. **6**, e16218 (2017).

[48] P. Zhao, M. Reichert, S. Benis, D. J. Hagan, and E. W. Van Stryland, Temporal and polarization dependence of the nonlinear optical response of solvents, Optica **5**, 583 (2018).

[49] S. Linden, H. Gießen, and J. Kuhl, XFROG—a new method for amplitude and phase characterization of weak ultrashort pulses, Phys. Status Solidi (b) **206**, 119 (1998).

[50] R. Trebino, *Frequency-Resolved Optical Gating: The Measurement of Ultrashort Laser Pulses* (Springer Science and Business Media, Berlin, 2012).

[51] J. Bethge, A. Husakou, F. Mitschke, F. Noack, U. Griebner, G. Steinmeyer, and J. Herrmann, Two-octave supercontinuum generation in a water-filled photonic crystal fiber, Opt. Express **18**, 6230 (2010).